water

MDPI

Article

Particle-Scale Modeling of Water-Spray Dust Suppression in Underground Excavation: A Weighted DSMC Framework for Droplet–Dust Capture

Qiang Li [1], Jinghong Yan [1,*], Yuxin Kang [1], Xue'an Zhuang [2], Jingdao Fan [3] and Dan Ma [1,*]

[1] Key Laboratory of Deep Coal Resource Mining of Ministry of Education, School of Mines, China University of Mining and Technology, Xuzhou 221116, China; qiangli@cumt.edu.cn (Q.L.); kyuxin1988@cumt.edu.cn (Y.K.)
[2] China Coal Technology and Engineering Group Chongqing Research Institute Co., Ltd., Chongqing 400037, China; xueanzhuang@126.com
[3] Zhengzhou Higher Research Institute, Henan Polytechnic University, Zhengzhou 451464, China; fan_jd@hpu.edu.cn
* Correspondence: tb23020034a51@cumt.edu.cn (J.Y.); dan.ma@cumt.edu.cn (D.M.)

Abstract

Water spraying is widely used for dust suppression in underground excavation, but the particle-scale mechanisms governing droplet–dust collision and capture remain insufficiently understood. This study develops a weighted Direct Simulation Monte Carlo (DSMC) framework that tracks spray droplets and dust particles in a two-dimensional prescribed airflow field and models stochastic collision, capture, and agglomeration. The model reproduces the pressure-dependent macroscopic capture response observed experimentally, with relative deviations below 3% at water pressures of 6 MPa and above. Increasing water pressure improves atomization and spray penetration and increases the probability of droplet–dust collision. At higher water pressures, the increase in capture efficiency becomes smaller, and the water consumption continues to rise. A narrower droplet-size distribution increases the effective droplet number density and improves spatial matching with dust particles. Fine dust is more difficult to capture because its lower inertia enables it to follow airflow around droplets, whereas capture efficiency generally increases with particle size before stabilizing. Atomization and spray incidence angles primarily affect capture by altering the spray coverage, local droplet concentration, and collision distribution. The weighted DSMC framework provides a particle-scale approach for exploratory comparison of spray operating conditions and spray geometry under the prescribed model assumptions.

Keywords: weighted Direct Simulation Monte Carlo (DSMC); spray dust suppression; droplet–dust collision; dust-capture efficiency; particle-scale modeling

Check for updates

Academic Editor: Gordon Huang

Received: 27 September 2026
Revised: 15 October 2026
Accepted: 20 October 2026
Published: 24 October 2026

Copyright: © 2026 by the authors. Licensee MDPI, Basel, Switzerland. This article is an open access article distributed under the terms and conditions of the Creative Commons Attribution (CC BY) license.

1. Introduction

Dust pollution remains a persistent occupational hazard in underground coal mining and mechanized roadway excavation. High-intensity cutting, crushing, loading, and transportation continuously generate large quantities of airborne particulate matter, among which the respirable fraction can penetrate deeply into the pulmonary system and is closely associated with coal workers' pneumoconiosis, silicosis, chronic obstructive pulmonary disease, and progressive massive fibrosis [1–3]. The resurgence of severe pneumoconiosis reported among coal miners in recent decades indicates that respirable-dust exposure remains an important occupational health concern despite advances in ventilation, monitoring, and personal protection [1–3]. Meanwhile, high-intensity mechanized mining can

generate large instantaneous dust loads and complex dust–airflow transport near working faces. Therefore, efficient capture of airborne dust, especially fine and respirable particles, remains important for improving underground working conditions [4,5].

Among the available engineering control measures, including ventilation, water infusion, foam, wet scrubbers, air curtains, and chemical dust suppressants, water spraying is one of the most widely used technologies because of its relatively low cost, simple equipment, rapid response, and suitability for installation close to dust-generating sources [4–6]. Spray dust suppression is governed by the relative motion between airborne particles and atomized droplets, followed by collision, wetting, adhesion or agglomeration and subsequent removal from the air. Depending on the particle size and operating conditions, inertial impaction, interception, Brownian diffusion, and electrostatic effects may contribute to particle capture [4–6]. Conventional water spraying, however, is generally less effective for highly hydrophobic coal dust and fine respirable particles. Accordingly, surfactants, magnetized water, compound wetting agents, and bio-based suppressants have been investigated to improve droplet wettability and dust agglomeration [7–11]. Although surface properties affect whether droplet–particle contact ultimately results in adhesion, the relative motion, size matching, collision probability, and spatial interaction between droplets and dust particles remain fundamental factors governing spray-capture performance [5,6].

Previous studies have also examined the effects of spray atomization and spatial coverage on dust suppression. Experimental and numerical studies have shown that spraying pressure, nozzle geometry, installation angle, droplet-size distribution, airflow disturbance, and nozzle arrangement strongly influence droplet concentration, velocity, coverage, and dust-removal efficiency. Liu et al. investigated the effects of spraying pressure and nozzle-orifice diameter in an external spraying system for a roadheader and demonstrated the coupling among water pressure, droplet size, and dust-suppression performance [12]. Yang et al. further examined the combined effects of the spraying pressure and nozzle installation angle on atomization characteristics and spray coverage [13]. Xu et al. reported that increasing pressure initially produces substantial droplet refinement, whereas the marginal improvement decreases at higher pressures [14]. Similar pressure-dependent behavior has been observed in numerical simulations and engineering applications involving coal cutters, continuous miners, and tunnel excavation systems [15–18]. Various spray configurations and atomization devices have consequently been developed to improve spray coverage and dust interception [18–25]. At the particle scale, Xu et al. investigated the dynamic wetting and wrapping of individual coal particles by droplets and showed that the droplet-to-particle size ratio and impact velocity strongly affect spreading and encapsulation [26]. Experimental investigations of different nozzle systems have likewise demonstrated that the droplet-size distribution and spray structure are important for fine-dust removal [27–30]. These studies show that dust capture is controlled by the droplet number density, droplet–dust size matching, relative velocity, and spray coverage, rather than by spray pressure alone. Respirable particles have low inertia and can more readily follow airflow streamlines around droplets, which reduces the probability of inertial collision [5,6,9].

Eulerian–Lagrangian approaches solve or prescribe the carrier flow and track dispersed particles, whereas DSMC provides a stochastic treatment of their collisions. These approaches are complementary rather than mutually exclusive: a DSMC collision module can be embedded in an Eulerian–Lagrangian transport model [31,32]. Engineering-scale approaches discussed above emphasize transport, concentration, and spray coverage; their treatment of droplet–dust interaction depends on the adopted collision and adhesion closures. The present implementation explicitly records sampled droplet–dust encounters and updates aggregate properties and statistical weights, but prescribes the airflow and omits

turbulence resolution and phase feedback. It consequently provides event-level collision information at the cost of a simplified flow representation; it is not inherently more accurate than a coupled CFD model.

The Direct Simulation Monte Carlo (DSMC) method provides a suitable stochastic framework for this purpose. Rather than deterministically examining every possible particle pair, DSMC statistically samples collision partners according to local particle number density, particle size, and relative velocity, allowing a large physical particle population to be represented by a computationally tractable number of sampled particles. DSMC-based collision algorithms have previously been applied to spray and particle-laden multiphase systems. Pawar et al. employed a stochastic DSMC algorithm to simulate droplet–droplet interactions in a liquid spray and validated the predicted spray evolution against experiments [31]. Finotello et al. combined an Eulerian–Lagrangian formulation, turbulent dispersion, and DSMC to investigate collision, coalescence, and separation in sprays [32]. Zhao et al. subsequently extended DSMC to liquid–solid mixed-phase agglomeration and demonstrated its capability for describing collision-induced aggregate formation and evolution [33]. Monte Carlo collision methods have also been used to sample particle or droplet interactions without evaluating every possible pair [34,35]. Previous DSMC studies have mainly addressed droplet–droplet collision, general spray systems, and liquid–solid agglomeration, whereas roadheader spray dust capture has received less attention. Therefore, this study applies a weighted DSMC collision model to roadheader spray dust suppression and evaluates its response to key spray parameters against experimental measurements.

This study develops a weighted DSMC model for spray dust suppression in the external spraying region of a roadheader. The framework integrates pressure-dependent spray injection, particle transport in a prescribed two-dimensional airflow field, stochastic collision sampling, and aggregate updating, with accepted collisions counted as capture under a unit sticking-probability assumption. The calculated overall capture fractions are compared with experimental dust-removal efficiencies across a range of spray pressures. One-factor simulations are then used to examine the effects of water pressure, droplet-size distribution, dust particle size, atomization angle, and spray incidence angle. Both time-dependent capture fractions and spatial collision distributions are analyzed to relate the reported trends to spray–dust overlap, while pressure-dependent water consumption is evaluated alongside capture performance. This work provides a particle-scale perspective for assessing spray operating conditions and nozzle arrangements in dust-control technology.

2. Methods

A DSMC-based particle framework was developed to investigate the interaction between spray droplets and airborne dust in the external spraying region of a roadheader. The numerical procedure consists of four coupled components: particle transport in the prescribed airflow field, spray-droplet generation, stochastic droplet–dust collision determination, and collision-induced capture and agglomeration. A weighted-particle treatment is employed so that a computationally tractable number of sampled particles can statistically represent the much larger number of physical droplets and dust particles. The model is subsequently evaluated against measurements obtained from a simulated roadway spray dust-suppression system.

2.1. Physical Model and Assumptions

The capture of airborne dust by water spray can involve inertial impaction, interception, Brownian diffusion, electrostatic attraction, wetting, and adhesion. Among these mechanisms, inertial collision associated with the relative motion between droplets and

dust particles is the principal mechanism explicitly resolved in the present model. As illustrated in Figure 1, sufficiently large dust particles deviate less readily with the surrounding airflow because of their inertia and can therefore collide with droplets located along their trajectories. Fine particles have lower inertia and can more readily follow the carrier airflow around droplets, resulting in a lower probability of inertial collision [5,6,26].

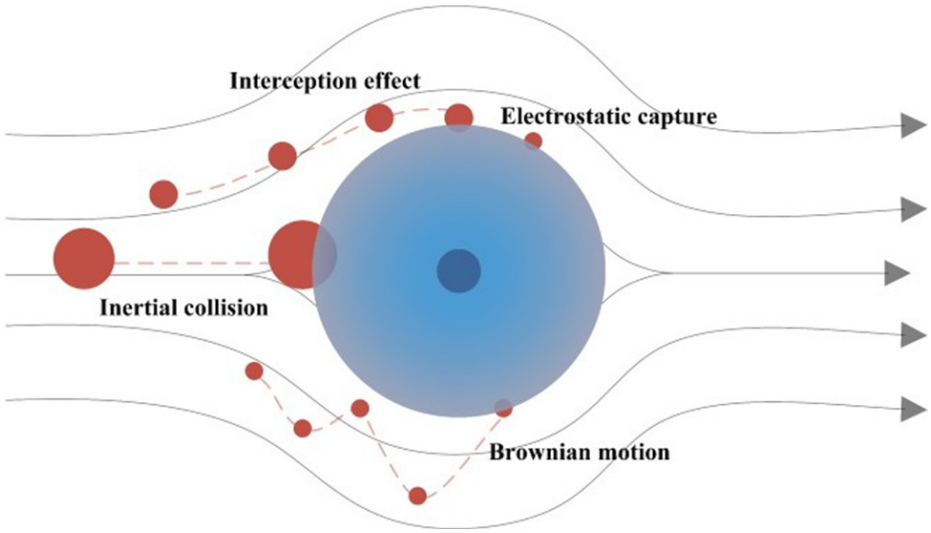


Figure 1. Mechanisms associated with spray capture of dust particles.

The present model focuses on the stochastic collision and subsequent capture process rather than explicitly resolving all microscale wetting and surface-interaction mechanisms. Accordingly, the following assumptions are adopted.

(1) Spray droplets and dust particles are treated as spherical particles; their projections in the two-dimensional computational domain are represented as circles. Particle rotation is neglected. The physical properties of the air, water, and dust are assumed to remain constant during each simulation.

The numerical dust-particle density is set to 2.5×10^3 kg/m^3 (Table 1). Because the validation experiment uses granite dust as the surrogate particulate material, this density is treated here as a mineral-dust surrogate parameter rather than as a coal-specific material property. Consequently, the reported quantitative predictions are interpreted for the adopted surrogate material, while coal-specific density and surface wetting effects are outside the present validation.

(2) An accepted droplet–dust collision is counted as capture under an assumed sticking probability of unity. The interaction is represented as perfectly inelastic, with conservation of represented mass and linear momentum. This is a collision-controlled closure, not a demonstrated criterion for stable wet adhesion. Rebound, splashing, partial attachment, and post-impact breakup are omitted. For the same modeled encounters, unit sticking maximizes the attached fraction, but the resulting efficiency is not a general upper bound on real dust removal because other collision mechanisms are also omitted.

(3) The collision module considers droplet–dust and aggregate–dust interactions. Dust–dust agglomeration and droplet–droplet collisions are excluded to isolate cross-phase encounter statistics.

(4) Brownian diffusion and electrostatic interactions are not included. The results therefore describe collision-controlled capture through the modeled particle motion and geometric collision kernel. Predictions for the smallest geometric particle-size groups should not be interpreted as validated fine-dust removal efficiencies.

(5) Droplet evaporation and secondary breakup after injection are not modeled. The injected droplet sizes are retained until collision-induced aggregation occurs.

Table 1. Numerical parameters used in the simulations.

Parameter	Value	Unit
Computational domain	2×1	m
Cell size	1×1	mm
Effective out-of-plane depth	1	m
Total simulation duration	1.5	s
Particle time step	1×10^{-5}	s
Background airflow velocity	5	m/s
Air dynamic viscosity	1.82×10^{-5}	Pa·s
Air density	1.293	kg/m^3
Dust-particle density (surrogate)	2.5×10^3	kg/m^3
Water density	1.0×10^3	kg/m^3
Water surface tension	7.2×10^{-2}	N/m
Water dynamic viscosity	1.005×10^{-3}	Pa·s
Nozzle flow coefficient C_q	0.61	-
Nozzle diameter	1.5	mm
Dust particle diameter	0–90	μm
Water pressure	2, 4, 6, 8, 10	MPa
Atomization angle	20–70	°
Spray incidence angle	10–60	°
Rosin–Rammler shape factor	1, 2, 3	-
Gravitational acceleration	9.81	m/s^2
DSMC kinematic search radius	$r_{s,ij} = G_{ij}\Delta t$	m
Sampled spray/dust particle numbers	2000	-

The external spray arrangement of a roadheader is illustrated in Figure 2a. The space between the atomizing nozzle and the excavation wall is extracted as the computational domain. As shown in Figure 2b, a two-dimensional rectangular region of 2 m × 1 m is employed. A Cartesian coordinate system is defined, with the excavation wall and dust injection boundary on the left side and the spray nozzle on the right side. The domain is discretized using square cells of 1 mm × 1 mm, corresponding to $2000 \times 1000 = 2.0 \times 10^6$ cells.

To provide the effective physical volume required for evaluating particle number density in the DSMC calculation, the two-dimensional domain is interpreted as a representative slice with a unit out-of-plane depth of b = 1 m. Accordingly, a planar search area A_s corresponds to an effective physical volume $V_s = A_s\, b$, and the local physical number density is evaluated as $n = (sum\ w_k)/V_s$, where w_k is the statistical weight of sampled particle k. This unit-depth convention is used consistently throughout the DSMC collision calculation.

The two-dimensional model represents the characteristic plane containing the principal directions of dust transport and spray propagation. It is used to analyze particle trajectories, spray coverage, and the spatial distribution of stochastic collision events while substantially reducing the computational cost relative to a fully three-dimensional simulation. The hard-sphere collision kernel is evaluated using the physical particle diameters and particle number density so that the stochastic collision calculation represents the corresponding physical particle population. The 1 mm square grid is solely a spatial index. It neither discretizes flow equations nor defines physical collision-mixing cells. Neighbor searches cover all intersected cells and apply the pair-distance criterion across cell boundaries. Complete, duplicate-free retrieval gives the same candidate set for different index sizes; this does not establish time step or particle number independence.

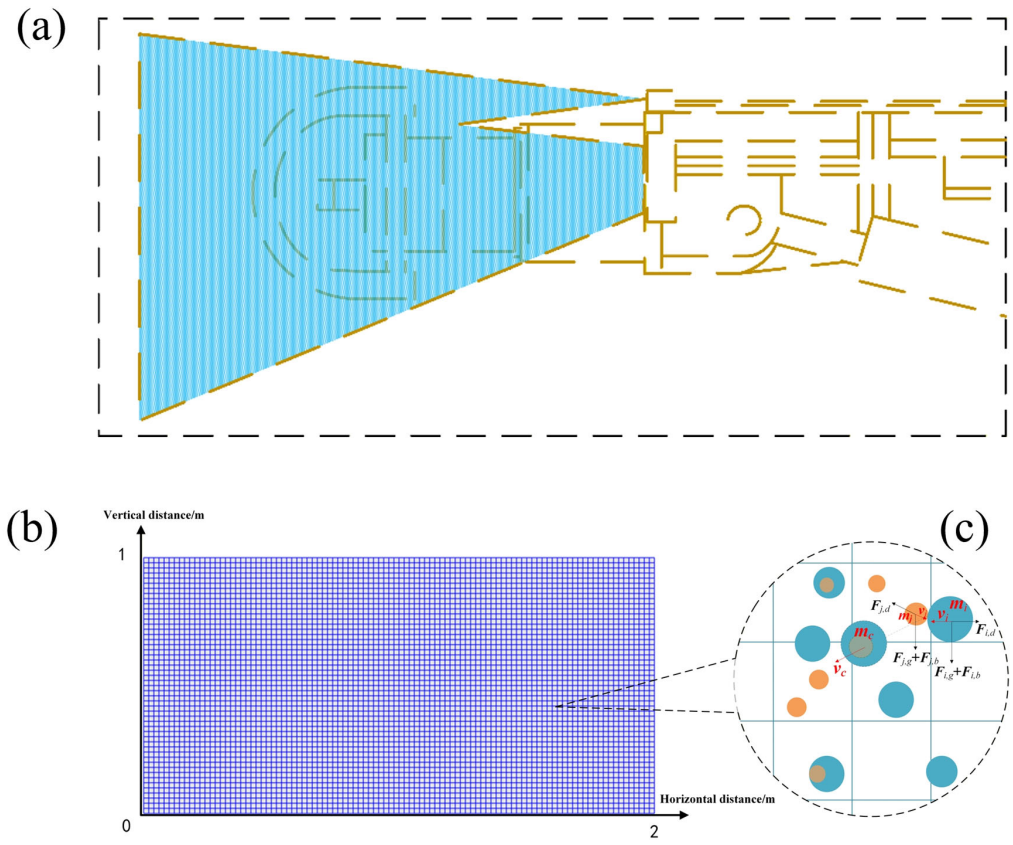


Figure 2. Establishment of the physical model: (**a**) external spray system of the roadheader; (**b**) computational domain and discretization; (**c**) schematic representation of particle collision and coalescence.

2.2. Continuous-Phase Airflow Model

Because the present model focuses on particle-scale collision and capture, the detailed turbulent structure of the roadway airflow is not resolved. The continuous phase is therefore represented by a prescribed airflow field. The background airflow velocity is set to 5 m/s, consistent with the operating condition used in the experimental system. The air density and dynamic viscosity are taken as 1.293 kg/m^3 and 1.82 $\times$ 10^{-5} Pa·s, respectively. The carrier airflow is prescribed as a steady, spatially uniform field throughout the two-dimensional computational domain. Taking the positive x-direction from the left-hand dust-injection boundary toward the right-hand spray nozzle side and the y-direction as vertical, the airflow velocity is specified as $u_x(x, y, t) = 5$ m/s and $u_y(x, y, t) = 0$ m/s. These components remain constant over the simulation period and are used to evaluate the aerodynamic drag on each particle. No airflow governing equations are solved. Turbulent fluctuations, local recirculation, and flow deflection around solid boundaries and individual droplets are not resolved. One-way coupling is assumed, so particle motion responds to the prescribed airflow without modifying it. This idealization provides a common background transport condition for comparing spray parameters.

Under this treatment, the dispersed particles respond to the continuous phase through aerodynamic drag, whereas feedback from the droplets and dust particles to the airflow is neglected. The numerical framework therefore represents one-way coupling between the prescribed continuous phase and the dispersed particles rather than a fully two-way coupled CFD calculation. This simplification allows the effects of water pressure, particle size, and spray geometry to be compared under the same prescribed airflow field.

2.3. Particle Motion and Boundary Treatment

The translational motion of each sampled particle is obtained from

$$\frac{d\mathbf{x}_p}{dt} = \mathbf{v}_p \tag{1}$$

and

$$m_p \frac{d\mathbf{v}_p}{dt} = \mathbf{F}_{D,p} + m_p \mathbf{g} \tag{2}$$

where the particle position, velocity, and mass denote the position, velocity, and mass of particle p, respectively; the aerodynamic drag force is denoted by $F_{D,p}$; and g is gravitational acceleration.

For a spherical particle, the drag force is expressed in the general form

$$\mathbf{F}_{D,p} = \frac{1}{2} C_D \rho_g A_p |\mathbf{u}_g - \mathbf{v}_p| (\mathbf{u}_g - \mathbf{v}_p) \tag{3}$$

where C_D denotes the drag coefficient; the remaining quantities denote the air density, projected particle area, particle diameter, and local airflow velocity, respectively. The particle Reynolds number is

$$Re_p = \frac{\rho_g d_p |\mathbf{u}_g - \mathbf{v}_p|}{\mu_g} \tag{4}$$

where the denominator contains the dynamic viscosity of air. The drag coefficient C_D is evaluated using the Schiller–Naumann correlation [36]:

$$C_D = \begin{cases} \frac{24\left(1+0.15 Re_p^{0.687}\right)}{Re_p}, & Re_p \le 1000 \\ 0.44, & Re_p > 1000 \end{cases} \tag{5}$$

The dust phase is initialized as a finite particle cloud rather than supplied through a continuous boundary source. At the start of particle tracking, 2000 computational dust particles are distributed independently and uniformly over the rectangular region $x = 0.10$–0.50 m and $y = 0.55$–0.95 m. Their initial velocity components are $v_{x,t} = 5\mathrm{m/s}$ and $v_{y,t} = 0$. No additional dust particles are generated during subsequent time stepping. The dust material density is 2500 $\mathrm{kg/m^3}$.

Particles are advanced using a particle time step of 1×10^{-5} s. Particles crossing an open boundary are classified as escaped and removed from subsequent calculations. Spray droplets and liquid–solid aggregates reaching the excavation wall are treated as deposited and removed from the computational domain. Dust particles leaving the domain without undergoing a droplet–dust capture event are classified as uncaptured. Meanwhile, all cases use the same particle number, time step, and random seed to keep the comparison consistent. Common random numbers can reduce random variation in comparisons when the random draws are properly matched across cases [37,38].

2.4. Spray Injection and Droplet-Size Distribution

Water supplied by the high-pressure pump is discharged through the atomizing nozzle. The volumetric flow rate is determined from the nozzle pressure according to [39]

$$Q = C_q \frac{\pi d_n^2}{4} \sqrt{\frac{2p}{\rho_l}} \tag{6}$$

where Q is the volumetric flow rate, C_q is the nozzle flow coefficient, d_n is the nozzle diameter, p is the water-supply pressure, and ρ_l is the liquid density. When SI units are used in Equation (6), d_n and p are expressed in m and Pa, respectively.

The initial axial spray velocity is correspondingly given by

$$v_0 = C_q \sqrt{\frac{2p}{\rho_l}} \tag{7}$$

When pressure is entered in MPa, it is converted to Pa before Equation (7) is evaluated.

The characteristic droplet size generated by pressure atomization is calculated using the empirical relationship [39]

$$\log_{10}\left(\frac{D_{50}}{\delta}\right) = 4.47La^{-0.133} - 0.35\log_{10}(We) \tag{8}$$

where D_{50} is the median droplet diameter predicted by the atomization correlation, δ is the characteristic dimension of the liquid sheet or jet, La is the Laplace number, and We is the Weber number.

The characteristic dimension is calculated from

$$\delta = \frac{d_n\left[1 - \sqrt{1 - C_q\cos(\alpha/2)}\right]}{2\cos(\alpha/2)} \tag{9}$$

where α is the atomization angle. The Laplace number is

$$La = \frac{\rho_l \sigma \delta}{\mu_l^2} \tag{10}$$

and the Weber number is

$$We = \frac{\rho_l v_0^2 \delta}{\sigma} \tag{11}$$

where σ and the liquid dynamic viscosity are the surface tension and dynamic viscosity of water, respectively. Appropriate unit conversion is applied when δ is entered in millimeters.

A single droplet diameter is insufficient to characterize an atomized spray. Therefore, the injected droplets are sampled from a Rosin–Rammler distribution. To retain D_{50} explicitly as the median diameter, the cumulative droplet-size distribution is written as

$$F(d) = 1 - \exp\left[-\ln(2)\left(\frac{d}{D_{50}}\right)^n\right] \tag{12}$$

where $F(d)$ is the cumulative fraction of droplets with diameters not exceeding d, and n is the Rosin–Rammler shape factor. Increasing n narrows the size distribution around D_{50}, whereas a smaller n produces a broader distribution. Shape factors of n = 1, 2, and 3 are examined in the parametric simulations [39,40].

The spray mass flow rate is the product of the liquid density and volumetric flow rate. Sampled spray particles are generated according to Equation (12), and each computational particle is assigned a statistical weight w, representing the number of physical droplets associated with that sampled particle. In this manner, variations in water pressure simultaneously affect the volumetric flow rate, droplet injection velocity, characteristic droplet size, and physical droplet population represented in the computational domain.

The principal numerical parameters used in this study are summarized in Table 1.

2.5. DSMC Collision Algorithm and Particle Weighting

Deterministic detection of every physical droplet–dust collision would be computationally prohibitive because the number of droplets and dust particles is extremely large. The DSMC method reduces this computational burden by tracking a smaller number of

representative particles and determining collision events statistically according to the local particle population, collision cross-section, and relative velocity [31–35].

Each sampled particle i is assigned a statistical weight w_i, which denotes the number of corresponding physical particles represented by that computational particle. Particle motion and collision are separated within each particle time step. During the motion stage, particle trajectories are updated according to Equations (1)–(4). During the collision stage, possible droplet–dust collision partners are searched within the local collision neighborhood, as schematically illustrated in Figure 3.

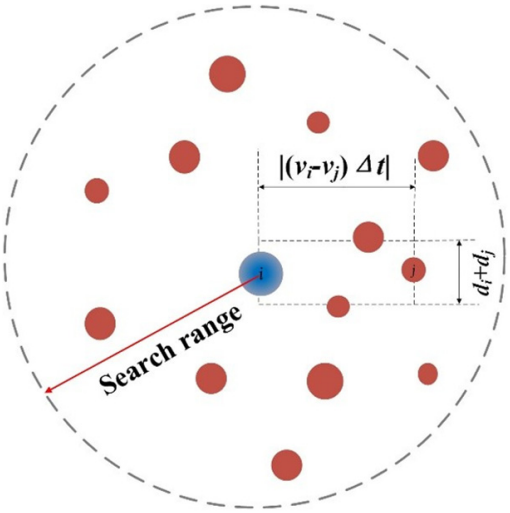


Figure 3. Schematic representation of DSMC collision determination between sampled particles.

For a spray particle i and a candidate dust particle j, the hard-sphere collision kernel is

$$K_{ij} = \frac{\pi}{4}(d_i + d_j)^2 G_{ij} \tag{13}$$

where $G_{ij} = |v_i - v_j|$ is the relative velocity between the two particles.

Let V_s denote the effective volume of the local search region defined in Section 2.1, containing N computational dust particles. Since candidate j represents w_j physical dust particles, the local physical number density is

$$n = \frac{\sum_{j=1}^{N} w_j}{V_s} \tag{14}$$

The mean statistical weight of these candidates is $\overline{w} = \frac{\sum_{j=1}^{N} w_j}{N}$. The physical number density represented by an average candidate is therefore

$$\frac{\overline{w}}{V_s} = \frac{n}{N} \tag{15}$$

Using the collision kernel in Equation (13), the collision swept volume over a time step Δt is $K_{ij}\Delta t$, assuming that the particle sizes and relative velocity remain approximately constant. Under a locally well-mixed approximation, the expected number of encounters of one physical droplet with the dust population represented by candidate j is $\frac{w_j}{V_s} K_{ij}\Delta t$. Replacing w_j with the mean weight $\overline{w}$ gives

$$\lambda_{ij} = \frac{\overline{w}}{V_s} K_{ij}\Delta t = \frac{n}{N} K_{ij}\Delta t \tag{16}$$

For locally Poisson-distributed encounters, the probability of at least one collision is $1 - \exp(-\lambda_{ij})$. When $\lambda_{ij} \ll 1$, its first-order approximation yields the weighted mean-density expression used in the reported calculations:

$$P_{ij} \approx \lambda_{ij} = \frac{n}{N}\frac{\pi}{4}(d_i + d_j)^2 G_{ij}\Delta t \tag{17}$$

The factor $\frac{n}{N}$ represents the average physical number density contributed by one computational candidate. This approximation replaces individual weight differences with their local mean; the density replacement is exact when all candidate dust particles have equal weights. For unequal weights, it remains an approximation and does not by itself establish the collision rate consistency of the complete parcel sampling procedure.

The random threshold acceptance test described in this formulation is mathematically equivalent to applying the probability bound

$$P_{\text{acc}} = \min(1, P_{\text{raw}}) \tag{18}$$

where the P_{raw} value is calculated from Equation (17). This treatment permits at most one accepted event per trial.

For each spray particle, the local candidate set is first constructed, one candidate j is sampled uniformly from the N candidates, and a uniformly distributed random number R between 0 and 1 is generated. The sampled collision is accepted when $R < P_{\text{acc}}$. After an accepted collision, the particle properties are updated using the capture and agglomeration procedure described in Section 2.6.

Because the search radius is proportional to the time step, changing the time step changes both particle advancement and the candidate neighborhood. A smaller displacement per step is therefore insufficient to establish convergence of the collision sampling. The sensitivity of this coupled procedure has not been quantified in the reported simulations.

The collision search radius is used as a kinematic sampling length rather than as a physical particle diameter or as a radius selected to enforce a prescribed candidate count. In the present formulation, $r_{s,ij} = G_{ij}\Delta t$, so the search neighborhood scales with the one-step relative displacement of a particle pair. This definition retains local spatial information while restricting candidate selection to the relative motion scale represented by the particle time step. The particle time step is $\Delta t = 1 \times 10^{-5}$ s.

Only droplet–dust and aggregate–dust interactions are included in the collision search procedure. Dust–dust and droplet–droplet collisions are excluded in accordance with the assumptions described in Section 2.1.

2.6. Droplet–Dust Capture and Agglomerate Treatment

Once a droplet–dust collision is accepted by the DSMC procedure, the two physical particles are assumed to undergo complete capture and form a liquid–solid aggregate. For a colliding spray droplet i and dust particle j, conservation of mass gives

$$m_c = m_i + m_j \tag{19}$$

where m_c is the mass of the resulting aggregate. Conservation of linear momentum gives

$$\mathbf{v}_c = \frac{m_i\mathbf{v}_i + m_j\mathbf{v}_j}{m_i + m_j} \tag{20}$$

where v_c is the post-collision aggregate velocity. Equation (20) corresponds to a perfectly inelastic capture event. The kinetic energy lost during the collision is therefore interpreted

as energy dissipated through droplet deformation, viscous effects, wetting, and adhesion and is not separately resolved.

To allow the newly formed aggregate to participate consistently in subsequent transport and collision calculations, its volume-equivalent diameter is updated according to volume addition

$$d_c = \left(d_i^3 + d_j^3\right)^{1/3} \tag{21}$$

and its effective density becomes

$$\rho_c = \frac{6\left(m_i + m_j\right)}{\pi d_c^3} \tag{22}$$

The resulting values of d_c, ρ_c, and v_c are then used in the subsequent particle motion and DSMC collision calculations.

Because one sampled particle can represent many physical particles, the collision between two computational particles does not imply that all of the physical particles represented by both parcels necessarily collide. If sampled particles i and j have statistical weights w_i and w_j, respectively, the number of physical collision capture events represented by their interaction is

$$w_c = \min\left(w_i, w_j\right) \tag{23}$$

When $w_i > w_j$, w_j physical droplets represented by particle i participate in the collision, whereas $w_i - w_j$ droplets remain uncollided. The sampled dust particle represents w_j newly formed aggregates with the properties calculated from Equations (19)–(22), while the remaining spray population retains its original properties.

Conversely, when $w_i < w_j$, all w_i droplets represented by particle i participate in capture, producing w_i aggregates, whereas $w_j - w_i$ dust particles remain uncaptured. The statistical weights of the corresponding computational particles are adjusted so that the total represented mass is conserved without requiring deterministic tracking of every physical particle. When $w_i = w_j$, the complete represented populations of both sampled particles participate in the collision.

The statistical weights are updated to conserve the represented mass without increasing the number of computational particles after each collision. Importantly, an aggregate formed by a previous collision retains its updated mass, equivalent diameter, density, velocity, and statistical weight and can subsequently collide with additional dust particles [33,34].

For Equation (23), dust involved in an accepted droplet–dust collision is counted as captured and remains classified as captured during subsequent aggregate motion. The subsequent trajectory of the resulting liquid–solid aggregate is tracked to account for further aggregate–dust collisions, but does not reverse the capture status assigned to the previously captured dust.

The instantaneous or final numerical dust-capture efficiency is evaluated from the weighted dust population, using a mass-based definition consistent with the experimental dust-concentration measurement

$$\eta = \frac{\sum\limits_{j \in \text{captured}} w_j m_j}{\sum\limits_{j \in \text{injected}} w_j m_j} \times 100\% \tag{24}$$

The numerical efficiency in Equation (24) is the fraction of injected dust mass assigned to accepted collision events, evaluated using the statistical weights. It is a mass-based collision-controlled capture metric under unit sticking. The experimental metric is inlet–

outlet dust-mass removal after the treatment region. Although both are mass fractions, their equivalence requires additional assumptions about adhesion, aggregate removal, and measurement response. For simulations in which all dust particles in a tested group have the same diameter, Equation (24) is equivalent to a weighted particle-number capture fraction.

2.7. Numerical Implementation and Parameter Variation

At the beginning of a simulation, the computational domain and continuous-phase airflow are initialized, and the dust and spray sampled-particle populations are generated according to the specified operating condition. Within each time step, the calculation proceeds sequentially through particle injection, particle transport, boundary treatment, local neighbor searching, stochastic collision determination, and collision-agglomeration updating. The updated particles are then advanced to the next time step. This procedure is repeated until the prescribed simulation duration of 1.5 s is reached.

The particle time step is 1×10^{-5} s. The same numerical settings are used for all parametric cases to minimize numerical differences between cases.

Five groups of operating parameters are investigated: water pressure, spray droplet-size distribution, dust-particle size, atomization angle, and spray incidence angle. Water pressures of 2, 4, 6, 8, and 10 MPa are considered. The Rosin–Rammler shape factor is varied from 1 to 3 to quantify the effect of droplet-size distribution uniformity. Dust particle diameters between 0 and 90 μm are analyzed in different size intervals. Atomization angles from 20° to 70° and spray incidence angles from 10° to 60° are considered. When one parameter is varied, the remaining parameters are maintained at the corresponding reference-condition values used for that parametric group.

For comparative simulations, the sampled-particle number, collision search procedure, and random-sampling settings are kept consistent; statistical weights are changed only when required by the physical loading. In the present calculations, 2000 sampled dust particles and 2000 sampled spray particles were used for each case, while the collision search radius was dynamically evaluated as $r_{s,ij} = G_{ij}\Delta t$.

2.8. Experimental Setup and Model Validation

The numerical framework was evaluated using a simulated roadway spray dust-suppression system at China University of Mining and Technology, as shown in Figure 4. The experimental apparatus reproduces the principal processes of dust generation, airflow-assisted transport, high-pressure spray interaction, mist removal, dust-concentration monitoring, and downstream extraction.

Dust is produced using an aerosol generator capable of providing a stable and controllable particle source. A disturbance fan positioned approximately 0.5 m downstream of the dust outlet promotes dispersion of the generated particles and reduces excessive local accumulation. The dispersed particles subsequently enter the main dust–spray interaction region, where a high-pressure nozzle connected to a pump and water tank generates the atomized spray. The pump provides a controllable water pressure of up to 12 MPa.

A demisting section is installed downstream of the interaction region to reduce the interference of suspended water droplets with the dust-concentration measurement. Dust-concentration sensors with a measurement range of 0–1000 mg/m^3 are positioned upstream and downstream of the spray-treatment region. An extraction system located at the downstream end provides airflow conditions of up to 5 m/s.

Granite dust is used as the experimental surrogate particulate material. The available material description provides the cumulative size thresholds summarized in Table 2: 50% below 10 μm, 80% below 80 μm, and 100% below 100 μm. Because the available description does not specify whether these cumulative percentages are mass-, volume-, or

number-based, the values are used here only as reported cumulative size constraints for the validation material and are not interpreted as a fully resolved particle-size distribution. The experimental comparison is therefore limited to the pressure-dependent macroscopic capture response and does not validate coal-specific wetting or adhesion behavior.

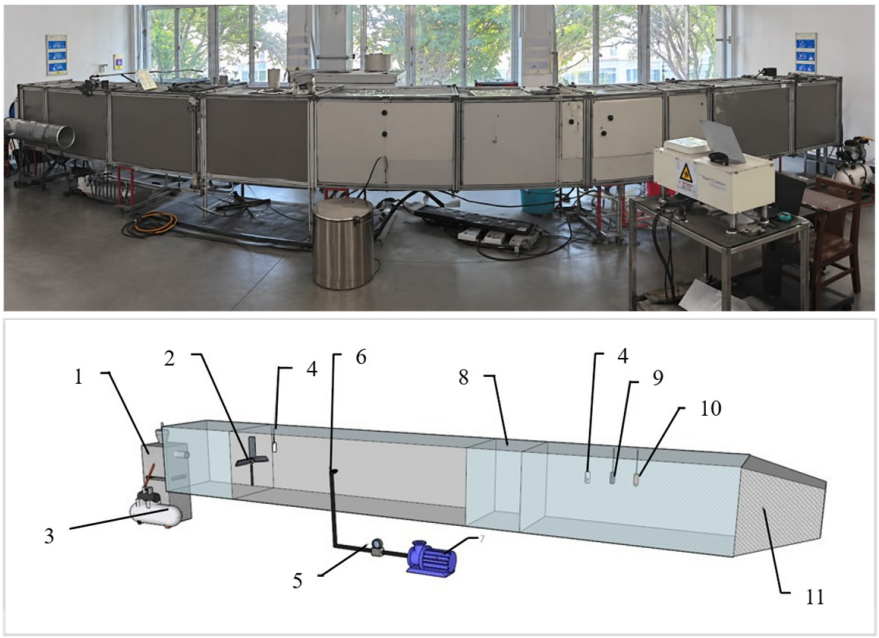


Figure 4. Simulated roadway spray dust-suppression experimental system. Note: 1—Aerosol Generator, 2—Turbulence Fan, 3—High-Pressure Air Pump, 4—TSP Dust-Concentration Sensor, 5—Pressure Gauge, 6—Nozzle, 7—High-Pressure Water Pump, 8—Demisting Chamber, 9—Wind Speed Sensor, 10—Temperature/Humidity Sensor, 11—Exhaust Fan.

Table 2. Cumulative particle-size distribution of the granite dust used in the experiment.

Particle Diameter Threshold	Cumulative Fraction (%)
<10 μm	50%
<80 μm	80%
<100 μm	100%

For each pressure condition, the spray pump is first operated and allowed to reach a stable spray state. The aerosol generator is then activated, and measurements begin after the dust flow becomes stable. Dust concentrations upstream and downstream of the spray-treatment region are recorded every 20 s. Three readings are obtained and averaged for each condition. The water pressure is increased successively from 2 to 10 MPa in increments of 2 MPa, and the measurement procedure is repeated after the system reaches a stable condition at each pressure. The three readings at each pressure are repeated observations within one test condition, rather than independent experimental runs.

The experimental dust-removal efficiency is calculated as

$$\eta_{\text{exp}} = \frac{C_{\text{in}} - C_{\text{out}}}{C_{\text{in}}} \times 100\% \tag{25}$$

where C_{in} and C_{out} are the measured dust mass concentrations before and after spray treatment, respectively. The relative deviation between the DSMC prediction and experimental result is calculated using

$$E_r = \frac{\left|\eta_{\text{DSMC}} - \eta_{\text{exp}}\right|}{\eta_{\text{exp}}} \times 100\% \tag{26}$$

As shown in Table 3, across 2, 4, 6, 8, and 10 MPa, the reported experimental efficiencies are 39.8%, 58.2%, 82.1%, 89.2%, and 93.8%, while the numerical values are 43.8%, 61.6%, 80.0%, 86.8%, and 91.6%. The corresponding relative deviations are 10.1%, 5.8%, 2.6%, 2.7%, and 2.3%; the numerical-minus-experimental differences are +4.0, +3.4, −2.1, −2.4, and −2.2 percentage points. The smaller deviations at higher pressures describe this aggregate comparison only; they are not uncertainty bounds.

Table 3. Comparison between numerical dust-capture efficiency and experimental dust-removal efficiency.

Pressure (MPa)	C_{in}	C_{out}	η_{exp}	η_{DSMC}	Error
2.0	245.6	147.8	39.8%	43.8%	10.1%
4.0	223.1	93.3	58.2%	61.6%	5.8%
6.0	215.8	38.6	82.1%	80.0%	2.6%
8.0	286.3	30.9	89.2%	86.8%	2.7%
10.0	216.2	13.4	93.8%	91.6%	2.3%

Note: Concentrations are reported as mean ± standard deviation (n = 3 readings per pressure condition).

The experimental comparison shows that the numerical framework reproduces the observed pressure-dependent trend in overall dust-removal efficiency. Because the available experiment measures the overall inlet–outlet dust concentration rather than individual droplet–dust collision events, it should not be interpreted as an independent direct validation of every microscale collision mechanism. The comparison therefore supports using the model for relative comparisons among the tested spray parameters, while not validating each microscale collision mechanism independently.

3. Results

3.1. Water Pressure and Capture Efficiency

In the present nozzle model, water pressure determines the volumetric flow rate, initial spray velocity, and characteristic droplet size. Figure 5 shows the particle distributions at different pressures, and Figure 6 compares the corresponding flow rate, spray velocity, characteristic droplet size, and capture efficiency.

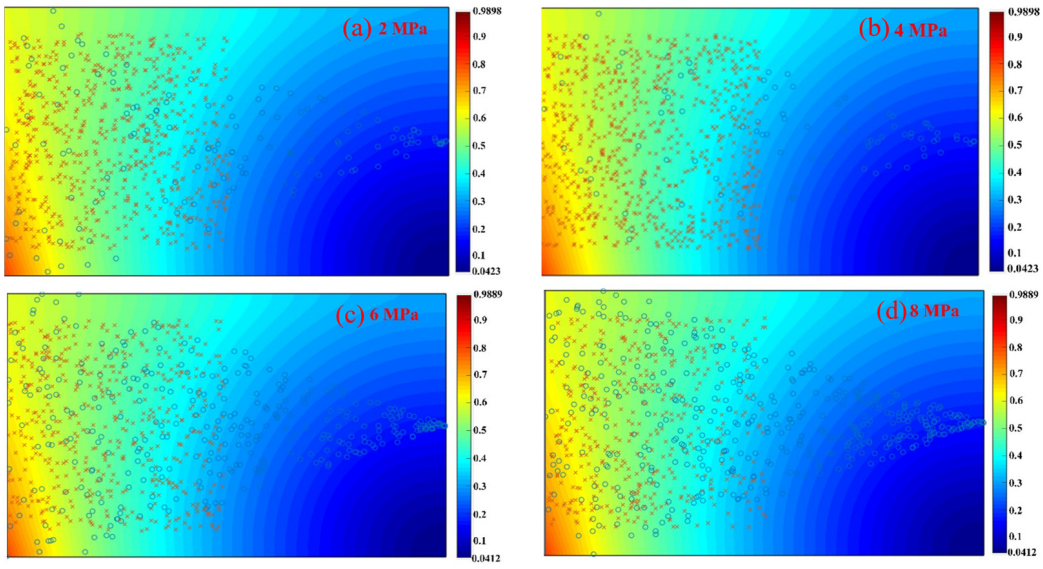


Figure 5. Schematic diagram of particle distribution under different water pressure conditions (○ represents the water droplet, × represents the dust particle).

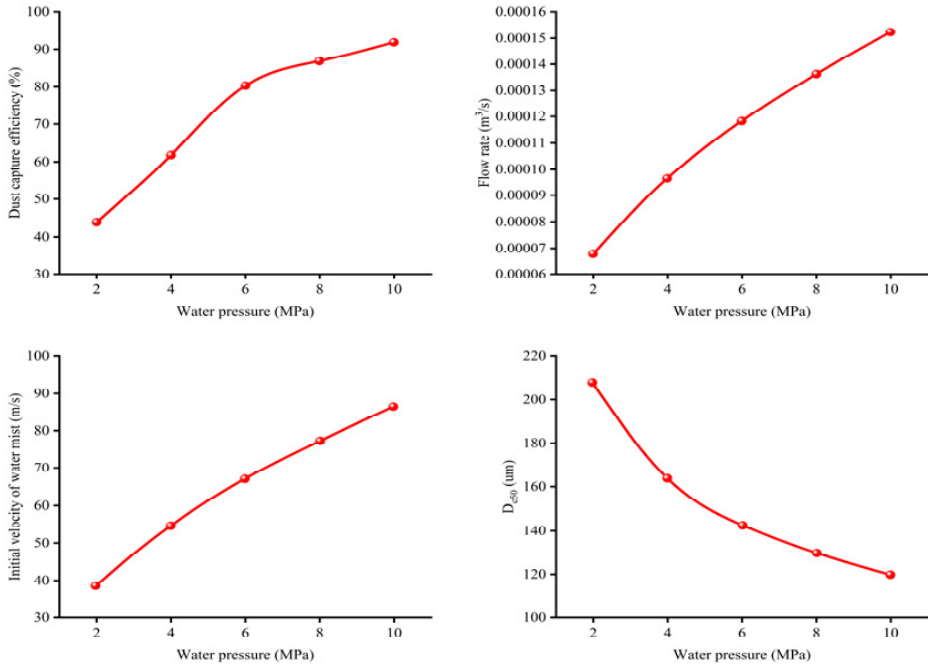


Figure 6. Dust-capture efficiency, volumetric flow rate, initial spray velocity, and D_{50} under different water pressures.

As water pressure increases, the spray–droplet density increases, and the main collision region moves toward the dust source. According to Equations (6) and (7), the volumetric flow rate and initial spray velocity increase with pressure. The characteristic droplet diameter decreases from 212 μm at 2 MPa to 144 μm at 6 MPa and 121 μm at 10 MPa. Over the same pressure range, capture efficiency increases from 43.8% to 80.0% and then to 91.6%. The increase in capture efficiency is therefore much larger from 2 to 6 MPa than from 6 to 10 MPa, whereas water consumption continues to increase with pressure. Using C_q = 0.61, d_n = 1.5 mm, and liquid density 1000 kg/m^3 in Equation (6), the calculated single-nozzle flow rates at 2, 4, 6, 8, and 10 MPa are 4.091, 5.785, 7.085, 8.181, and 9.147 L/min, equivalent to 245.4, 347.1, 425.1, 490.9, and 548.8 L/h.

The time-dependent capture efficiency under different water pressures is shown in Figure 7. At 2 MPa and 4 MPa, the efficiency increases almost linearly but with limited improvement; many dust particles remain uncaptured by the end. At 6 MPa and above, the capture effect is significant at early stages; most dust particles are captured in the early period, and only a few escape the spray coverage, causing efficiency to saturate later.

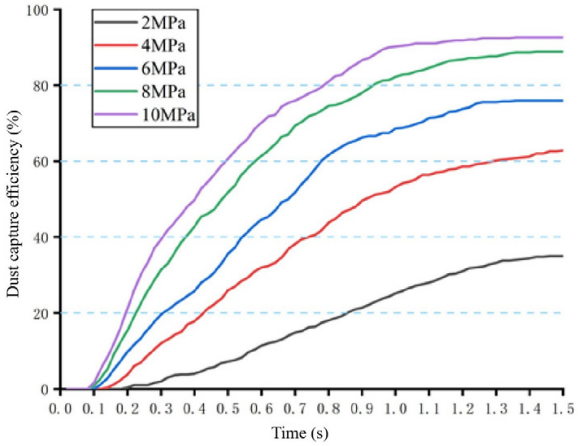


Figure 7. Changes in dust-capture efficiency over time under different water pressure conditions.

3.2. Particle Collision Distribution

After leaving the nozzle, the droplets form a conical spray region. Spray droplets collide with and capture dust particles within this region. The spatial collision distribution is therefore used to characterize where droplet–dust interactions occur.

Figure 8 shows the collision position and density distributions under different water pressures. Overall, most collisions occur within the conical spray-covered region, with fewer events at the periphery. As water pressure increases from 2 MPa to 4, 6, 8, and 10 MPa, the main collision zone shifts horizontally from 1.3–1.9 m to 0.9–1.5 m, 0.9–1.5 m, 0.7–1.3 m, and 0.7–1.3 m from the dust injection position, i.e., moving toward the rock wall (near the dust source). Higher pressure increases the initial droplet velocity and the number of droplets represented in the spray field. The higher initial velocity allows droplets to reach farther toward the dust-source side before being deflected by the airflow, increasing collision events in that region. The increased droplet number density also raises the number of potential droplet–dust encounters near the dust source. At low pressure, some smaller droplets with low initial velocity may deviate from the conical region under airflow, but they can still capture dust outside the main zone.

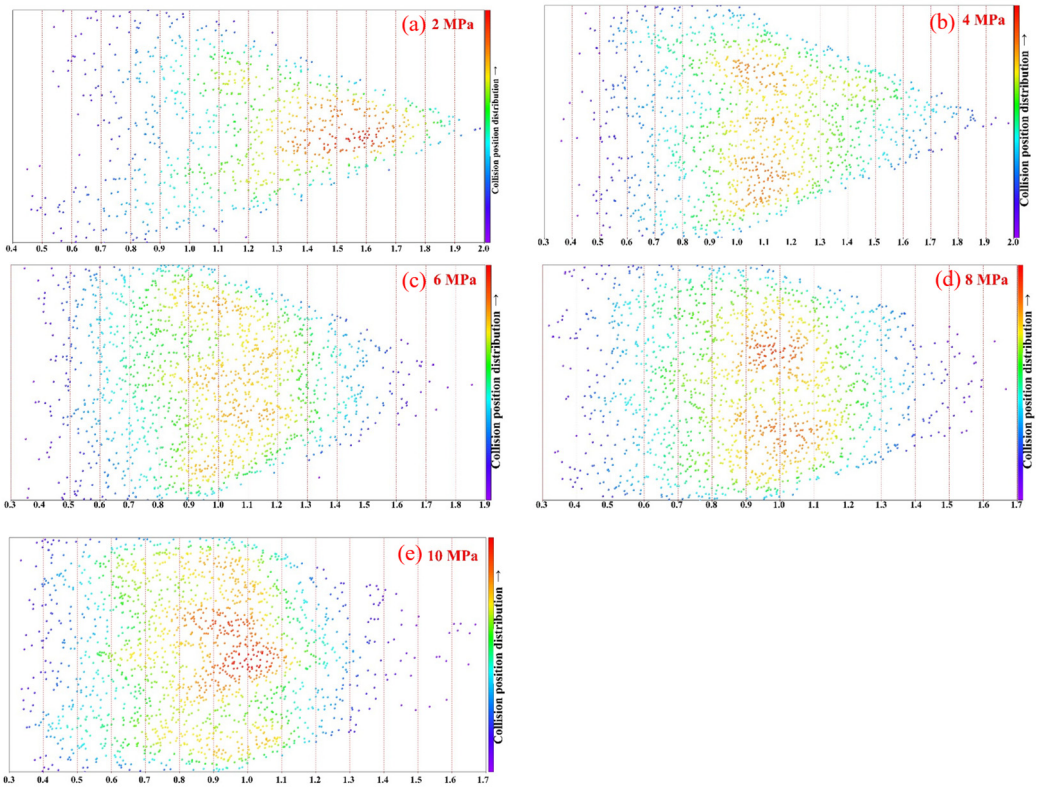


Figure 8. Spatial distributions of droplet–dust collision events at different water pressures: (**a**) 2 MPa; (**b**) 4 MPa; (**c**) 6 MPa; (**d**) 8 MPa; and (**e**) 10 MPa.

3.3. Spray Droplet Size Distribution and Capture Efficiency

The effect of droplet-size distribution uniformity is examined using the Rosin–Rammler distribution. The shape factor n is varied from 1 to 3. At each water pressure, D50 obtained from Equation (8) denotes the prescribed median droplet diameter. The cumulative sampling distribution can be written in the standard scale parameter form:

$$F(d) = 1 - exp\left[-\left(\frac{d}{x_c}\right)^n\right] \quad (27)$$

where $F(d)$ is the cumulative sampling distribution of droplet diameter d, x_c is the characteristic scale diameter, and n is the shape factor. The scale diameter and median diameter are related by:

$$x_c = \frac{D_{50}}{(ln\ 2)^{\frac{1}{n}}} \tag{28}$$

Substitution gives the median-based distribution in Equation (12). The droplet diameters used in the simulations were generated by inverse transform sampling:

$$d = D_{50}\left[\frac{-ln(1-U)}{ln\ 2}\right]^{\frac{1}{n}}, \quad U \sim Uniform(0,1) \tag{29}$$

where U is uniformly distributed over (0,1). Thus, the prescribed distribution satisfies $F(D_{50}) = 0.5$ for all three shape factors. Increasing n narrows the prescribed sampling distribution at the specified median.

Figure 9 illustrates the dust capture efficiency for different spray droplet size distributions under each water pressure. At all pressures, when shape factor n = 1, the droplet size distribution is broad, ranging from 0 to 1200 μm; when n = 2, sizes are more concentrated around 0–500 μm; when n = 3, the distribution is more uniform, around 0–400 μm. At 2 MPa, efficiencies for n = 1, 2, 3 are 16.5%, 41.15%, and 50.95%, respectively; at 4 MPa: 30.25%, 65.7%, 74.5%; at 6 MPa: 42.4%, 67.9%, 74.85%; at 8 MPa: 51.15%, 87.8%, 94.2%; and at 10 MPa: 59.2%, 90.8%, 94.6%. For the prescribed droplet spectra tested here, increasing n was associated with a higher simulated collision-controlled capture fraction. These results describe the response to the specified Rosin–Rammler distributions and should not be interpreted as a universal relationship between the distribution width and capture performance. A change in the represented physical droplet number cannot be inferred from n alone without considering the statistical weights used to impose the liquid loading.

3.4. Dust Particle Size and Capture Efficiency

Dust particles in excavation can span a wide size range; here, particle diameters from 0 to 90 μm are considered. Spray dust suppression has different capture efficiencies for different dust sizes.

With water pressures set at 2, 4, 6, 8, and 10 MPa, the capture efficiencies for different dust size ranges and their variation rates are shown in Figure 10a,b. At 2 MPa, as the dust size increases from 0–10 μm to 30–40 μm, efficiency rises from 28.6% to 30.4%, 33%, and 36.2%, with incremental increases of 6.29%, 8.55%, and 9.7%; from 30–40 μm to 80–90 μm, efficiency fluctuates around 37%. At 4 MPa, from 0–10 μm to 40–50 μm, efficiency first fluctuates around 54% then increases to about 60%, with changes of +3.8%, −1.1%, +12.59%, and −4.93%; from 40–50 μm to 80–90 μm, efficiency hovers around 62%. At 6 MPa, from 0–10 μm to 40–50 μm, efficiency increases from 73% to 74.4%, 78.2%, 80.9%, and 82.4%, with increments of 1.92%, 5.11%, 3.45%, and 1.85%; from 40–50 μm to 80–90 μm, it fluctuates slightly around 83%. At 8 MPa, from 0–10 μm to 40–50 μm, efficiency increases from 79% to 81%, 83.2%, 84.2%, and 87.2%; for sizes above 50 μm, it stays around 88%. At 10 MPa, from 0–10 μm to 30–40 μm, efficiency changes from 83.8% to 87.4%, 87.2%, and 91.4%, with increments of 4.3%, −0.23%, and 4.82%; from 30–40 μm to 80–90 μm, efficiency is generally around 93%.

For particles smaller than about 40 μm, the predicted capture efficiency generally increases with particle size. This trend is consistent with the increase in particle inertia, which reduces the tendency of dust particles to follow airflow streamlines around droplets. When the particle size exceeds about 40 μm, the capture efficiency changes only slightly under the present spray conditions. The fluctuations among particle-size classes are larger at low water pressure and decrease as water pressure increases.

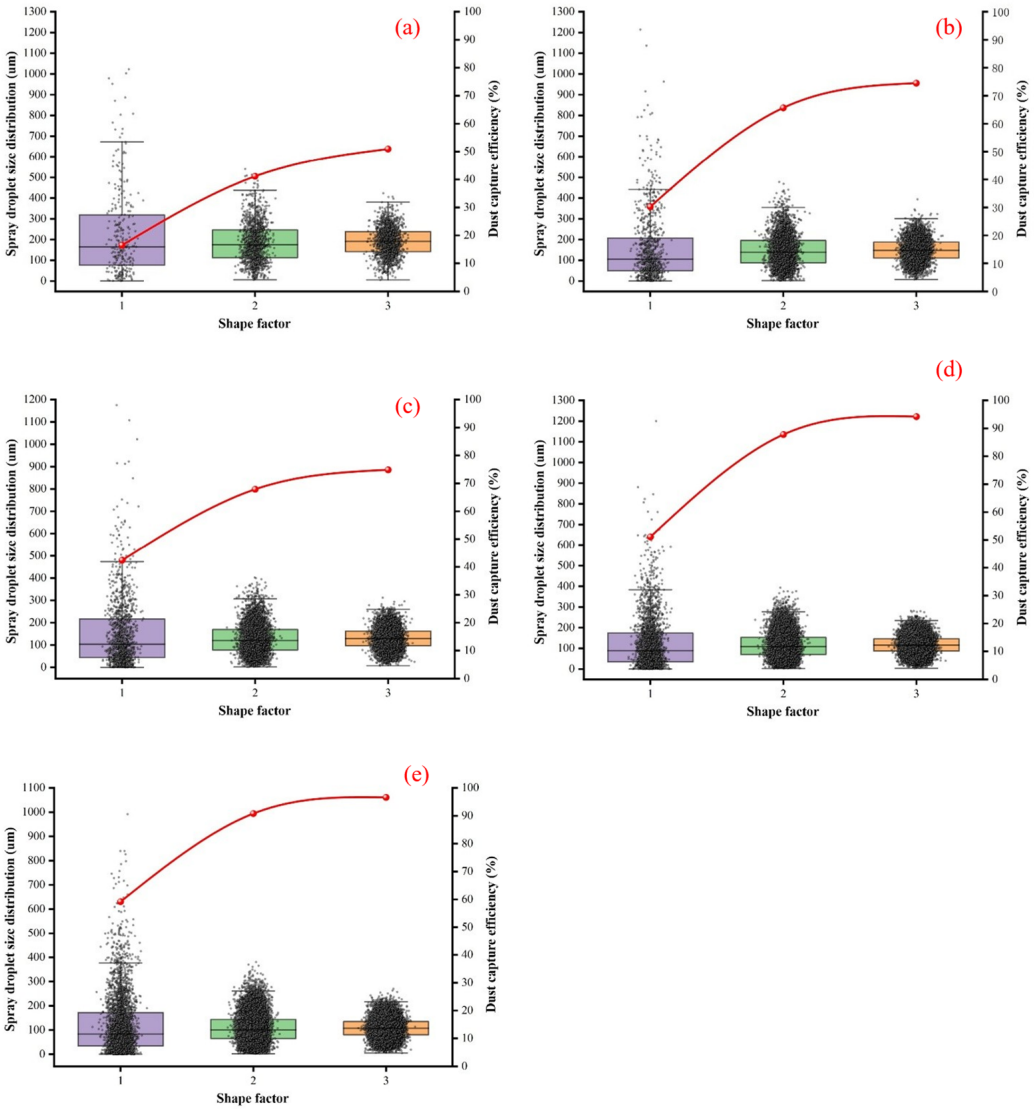


Figure 9. Effect of spray droplet-size distribution on dust-capture efficiency at different water pressures: (**a**) 2 MPa; (**b**) 4 MPa; (**c**) 6 MPa; (**d**) 8 MPa; and (**e**) 10 MPa. The red line represents the dust capture efficiency.

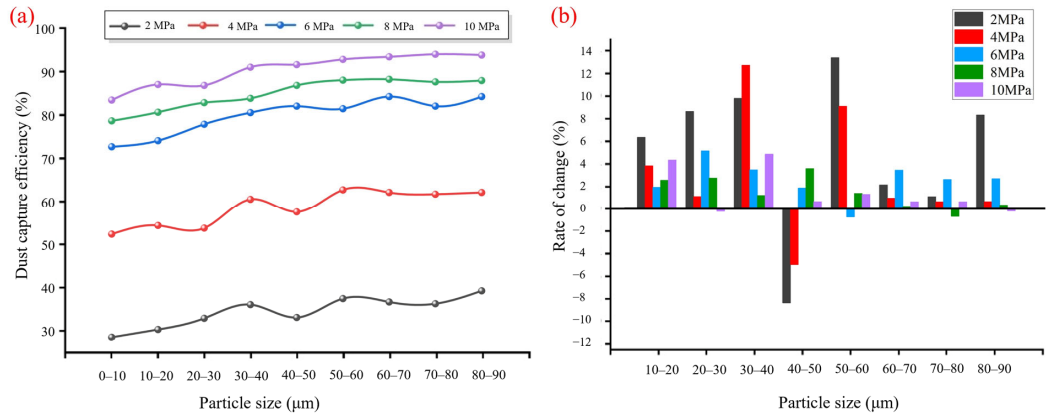


Figure 10. Influence of dust-particle size on dust-capture efficiency: (**a**) capture efficiency for different dust-particle sizes; (**b**) rate of change in capture efficiency with increasing particle size.

3.5. Spray Atomization Angle and Capture Efficiency

The effect of the atomization angle is evaluated at 8 MPa with a Rosin–Rammler shape factor of $n = 2$. Different atomization angles yield different capture efficiencies.

With water pressure at 8 MPa and shape factor $n = 2$, collision distributions for different atomization angles are shown in Figure 11. At 20°, the main collision zone is horizontally 0.3–1.5 m (closer to the dust injection side) and vertically 0.2–0.8 m, with very high-density collisions inside the spray cone. At 30° and 40°, the main collision zone shifts to 0.3–1.8 m horizontally, closer to the spray injection side, with a broader and more uniform distribution. At 50° and above, the main zone extends to 0.3–1.9 m, and the density inside the cone becomes similar to the periphery, indicating a very uniform collision distribution. A smaller atomization angle produces a higher collision density along the spray path but covers a smaller spatial region. As the angle increases, the collision region expands, while the local collision density decreases; the wider spray region captures dust over a larger area.

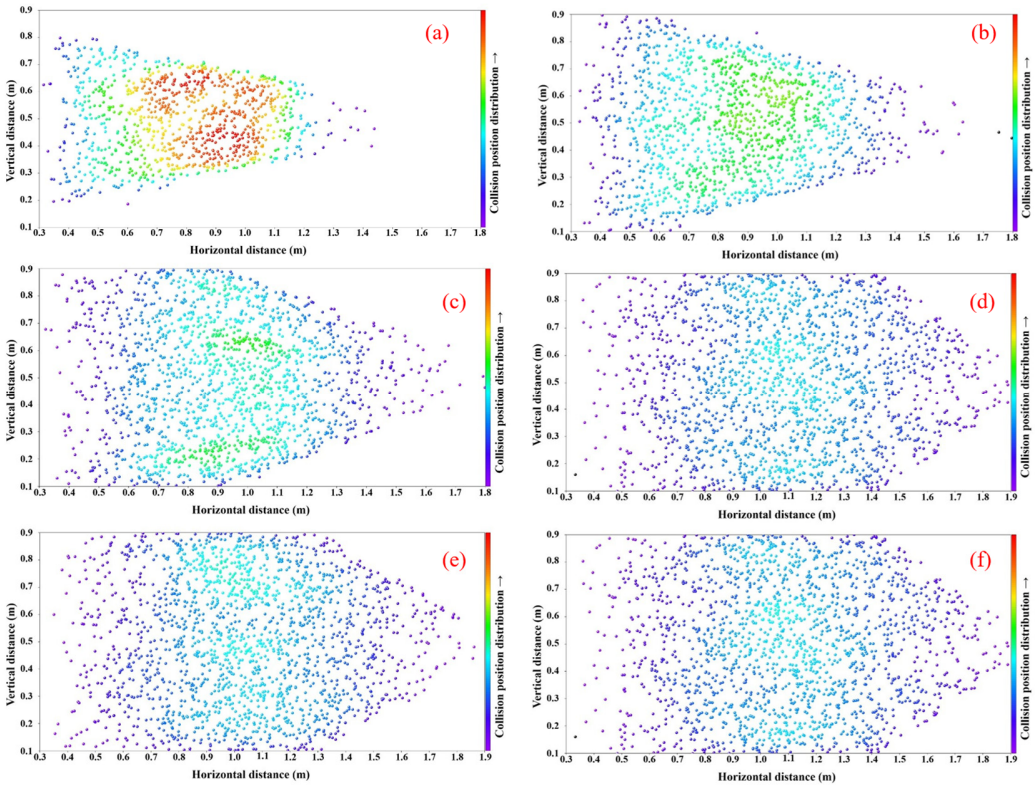


Figure 11. Droplet–dust collision distributions at different atomization angles: (**a**) 20°; (**b**) 30°; (**c**) 40°; (**d**) 50°; (**e**) 60°; and (**f**) 70°.

The time-dependent capture efficiency for different atomization angles is shown in Figure 12. At 20° and 40°, efficiency reaches saturation quickly, indicating rapid and efficient capture of dust along the spray path. At 50° and above, as the angle increases, the droplet density decreases, leading to lower initial capture efficiency compared to smaller angles; however, the larger coverage enables more dust to be captured later.

3.6. Spray Incidence Angle and Capture Efficiency

The nozzles mounted on the roadheader boom can often be rotated to adjust the spray incidence angle. Different incidence angles lead to distinctly different capture performance.

Collision distributions for different incidence angles are shown in Figure 13. At 10° and 20°, the collision pattern is similar to horizontal injection, with main collisions inside the conical region and most dust suppressed near the rock wall. At 30° and above, the

main collision zone shifts to the lower side of the cone, and the collision zone narrows. As the incidence angle increases, the main collision region moves away from the near-source zone and becomes more curtain-like across the dust transport path.

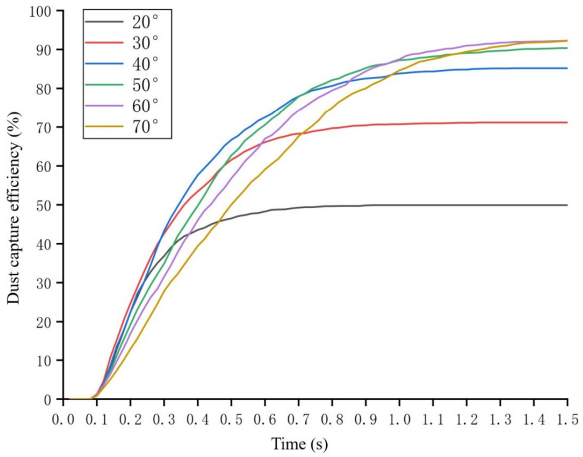


Figure 12. Changes in dust-capture efficiency over time under different atomization angles.

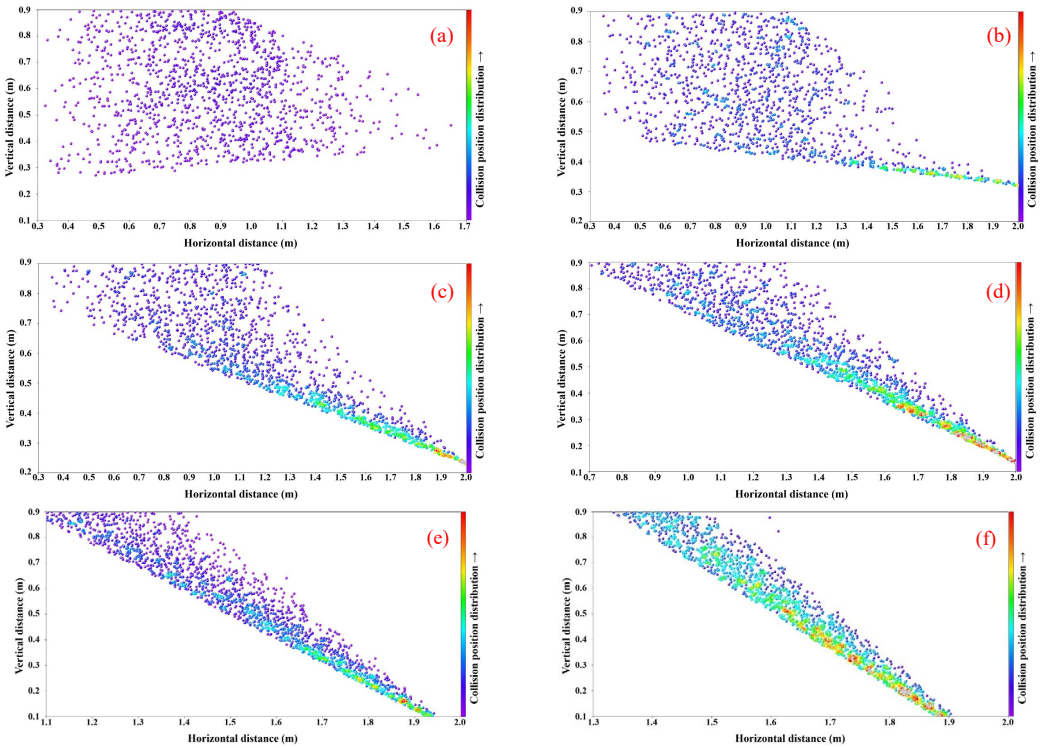


Figure 13. Droplet–dust collision distributions at different spray incidence angles: (**a**) 10°; (**b**) 20°; (**c**) 30°; (**d**) 40°; (**e**) 50°; and (**f**) 60°.

Figure 14 shows the time-dependent capture efficiency for different incidence angles. As the angle increases from 10° to 50°, the onset of collisions is delayed, while the final capture efficiency generally increases; at 60°, the final efficiency decreases slightly. A larger incidence angle increases the transverse overlap between the spray and the dust-transport path, which increases interception over a wider region. At 60°, the final capture efficiency is slightly lower than at 50°. This decrease may be related to the narrower vertical collision region and the larger number of collision events outside the main spray–dust interaction zone in Figure 13.

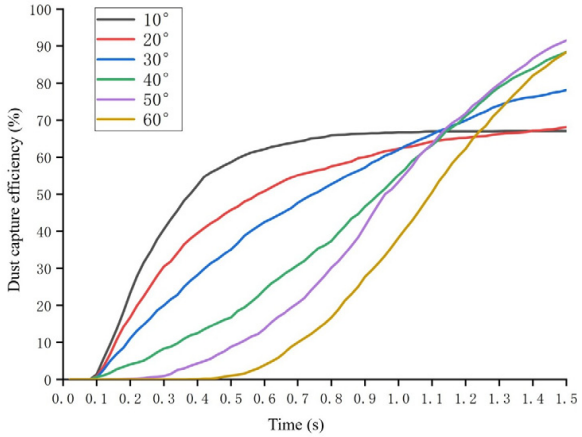


Figure 14. Time dependence of dust-capture efficiency at different spray incidence angles.

4. Discussion

4.1. Coupled Control Mechanisms of Spray Dust Capture

In the present model, dust capture is controlled by droplet–dust collision within the finite spray–dust interaction region. In the DSMC framework, the local collision probability mainly depends on the particle number density, collision cross-section, and relative velocity. The water pressure, droplet-size distribution, and dust-particle size affect the process in different ways. However, they all influence capture efficiency by changing the number of droplets, particle inertia, and the spatial overlap between droplets and dust particles. The observed pressure and particle-size trends are consistent with previous reports on spray atomization and droplet–dust size matching [12–14,26–30].

Water pressure first affects the number, size, and initial momentum of spray droplets. When the pressure increased from 2 MPa to 6 MPa, the characteristic droplet diameter decreased from 212 μm to 144 μm, while the capture efficiency increased from 43.8% to 80.0%. The main collision zone also shifted from 1.3 to 1.9 m at 2 MPa to 0.9 to 1.5 m at 4–6 MPa, and further shifted to 0.7–1.3 m at 8–10 MPa. These results show that increasing water pressure not only increases the number of droplets available for collision, but also improves spray penetration toward the dust source. As a result, the main dust-capture region gradually moves closer to the dust source.

When the pressure exceeded about 6 MPa, the benefit of further increasing the pressure became much smaller. When the pressure increased from 6 MPa to 10 MPa, the characteristic droplet diameter decreased only from 144 μm to 121 μm. The capture efficiency increased from 80.0% to 91.6%, while the hourly water consumption increased by 122 L. Above 6 MPa, capture efficiency increases more slowly, indicating diminishing returns under the tested conditions. The remaining uncaptured dust is mainly located outside regions with a high droplet collision density, as indicated by the collision distribution results. Thus, the incremental increase in capture efficiency becomes smaller at higher water pressures.

In the present simulations, capture efficiency rises by 36.2 percentage points from 2 to 6 MPa, compared with 11.6 percentage points from 6 to 10 MPa. Yang et al. [13] reported a mean overall dust-suppression efficiency of 90.10% for an external spray system operated at 8 MPa with 2.0 mm nozzles. The present 1.5 mm nozzle case gives a collision-controlled capture fraction of 86.8% at 8 MPa. Beck et al. [41] studied coal dust smaller than 75 μm in a 3.6 m/s airflow. For their FC59 full-cone spray, regression analysis estimated a 20.9 percentage-point efficiency increase as pressure rose from 0.552 to 1.103 MPa. These comparisons provide numerical context for the pressure effect. Differences in spray geometry, dust populations, airflow, and efficiency definitions limit direct comparison of absolute values.

The droplet-size distribution also has a strong effect on capture efficiency. At 4 MPa, increasing the Rosin–Rammler shape factor n from 1 to 3 increased the capture efficiency from 30.25% to 74.5%, indicating a substantial improvement in dust-capture performance. At 10 MPa, the capture efficiencies for n = 1 and n = 3 were 59.2% and 94.6%, respectively. A broad droplet-size distribution contains more large droplets. Large droplets occupy more liquid volume, so fewer physical droplets are formed at the same liquid flow rate. As the droplet-size distribution becomes narrower, the proportion of medium and small droplets increases. This increases the droplet number density and provides more opportunities for droplet–dust collisions. However, this conclusion is limited to the range of n = 1–3 investigated in this study. It does not mean that a narrower droplet-size distribution is always better under all conditions.

Dust-particle size mainly affects the collision process through particle inertia. For dust particles smaller than about 40 μm, the capture efficiency generally increases with particle size. Dust particles of 0–10 μm are the most difficult to capture, with a minimum predicted capture efficiency of only 28.6%. Fine particles have low inertia and can more easily follow the airflow around droplets. This reduces the probability of inertial collision [5,6,9]. As particle size increases, dust particles can more easily deviate from the airflow streamlines and collide with droplets. For particles larger than 40 μm, the capture efficiency gradually becomes stable. Under the tested spray conditions, increasing particle size beyond about 40 μm produces only small changes in capture efficiency.

4.2. Engineering Implications

Under the tested conditions, capture efficiency increases rapidly from 2 to 6 MPa and continues to increase above 6 MPa. However, the incremental improvement becomes smaller at higher pressures, while water consumption continues to rise. Under the present nozzle, airflow, and spray-geometry conditions, approximately 6 MPa marks the onset of a diminishing return regime rather than a universal optimum pressure. From a water-use perspective, further pressurization above this regime produces progressively smaller gains in dust capture while continuing to increase water demand. Pressure selection should therefore consider both dust-capture performance and water consumption, together with the required spray coverage.

At the same water pressure, changes in the droplet-size distribution can substantially affect capture efficiency, with the largest increase observed from 30.25% to 74.5%. This result shows that the droplet-size distribution strongly affects capture efficiency at the same water pressure. The Rosin–Rammler shape factor is not a parameter that can be directly adjusted in the field. Instead, it is an indicator used to describe the droplet-size distribution. The present results indicate that nozzle evaluation should include both the characteristic droplet size and the width of the droplet-size distribution.

Spray geometry mainly determines the spatial interaction between droplets and dust particles. A smaller atomization angle can increase the local droplet density along the spray path, but its coverage is limited. As the atomization angle increases, the collision region expands from about 0.3–1.5 m to 0.3–1.9 m. The spray coverage therefore becomes larger, but the local droplet density and initial capture rate decrease. Under the present geometry, the atomization angle controls the trade-off between collision density and spray coverage. A smaller angle increases local collision density, whereas a larger angle increases the spatial coverage of the spray.

The spray incidence angle determines whether the spray system mainly provides near-source dust suppression or spatial dust interception. At incidence angles of 10–20°, most collisions occur near the rock wall and the dust source. When the incidence angle increases to 30° or above, the spray gradually acts as a water curtain and intercepts suspended dust.

Within the tested geometry and operating conditions, the highest capture efficiency was obtained at 50°, reaching 91.5%, which was substantially higher than that at 10°. At 60°, the capture efficiency decreased slightly. For a concentrated near-wall dust source, the lower incidence angles in the present simulations produced more near-source collisions. For dust transported along a defined path, the present simulations show that a larger incidence angle increases the transverse interception range.

The minimum collision-controlled capture fraction for the 0–10 μm geometric size class is 28.6%. This value should be interpreted cautiously because Brownian diffusion and electrostatic interactions are omitted, and every accepted collision is assumed to result in capture without resolving wetting and adhesion. It is therefore a model result rather than a validated wet-removal efficiency. The geometric size class is not used as a direct measure of respirable-dust removal. Water pressure, droplet-size distribution, and spray geometry should be considered together when comparing the modeled spray conditions.

4.3. Limitations and Future Work

The present model still has several limitations. The computational domain is a 2 m × 1 m two-dimensional representative slice with a unit out-of-plane depth. The background airflow velocity is fixed at 5 m/s, and one-way coupling from the airflow to the particles is used. Accordingly, the present model is used for relative comparisons of particle transport and collision distributions under the prescribed airflow field. However, it cannot fully represent three-dimensional non-uniform turbulence, airflow around equipment, local recirculation, or two-way coupling between the spray and airflow in an actual roadway. Future work could couple the weighted DSMC framework with a three-dimensional transient CFD flow field. A three-dimensional transient flow field is needed to test whether the same collision trends persist under non-uniform roadway airflow.

The mean-density approximation and the probability bound introduce a numerical limitation. Saturation may alter the represented collision rate when the unbounded probability is large, so the results should be interpreted within this approximate collision-sampling formulation. Its quantitative accuracy requires further collision rate and time step sensitivity verification.

The omitted processes have different conditions of applicability. Droplet–droplet collision rates depend on the local droplet number density, size, and relative velocity [23]. Aerosol coagulation also requires comparison of transport and coagulation timescales; for a constant kernel, the latter is proportional to the inverse of the product of the kernel and particle number concentration [25].

Brownian diffusion is included in spray-scavenging models for submicron particles [33,35], while electrostatic experiments demonstrate that charge conditions can substantially alter fine-particle collection. Consequently, the present 0–10 μm results represent the modeled collision-controlled fraction rather than a validated wet-removal efficiency.

Each case was run once, so the variation between repeated runs is unknown. Tests with different particle numbers, time steps, and random seeds are needed to check their effects on capture efficiency and collision locations.

At the collision model level, Equation (14) employs a weighted mean-density candidate approximation, and the local search neighborhood is defined using the kinematic length $r_{s,ij} = G_{ij}\Delta t$. These choices are used for local stochastic sampling and relative parametric comparison; sensitivity to alternative candidate selection rules and neighborhood definitions should be examined in future model development.

The current model directly treats a droplet–dust collision identified by the DSMC procedure as a stable wet capture event. The collision is modeled as a perfectly inelastic collision. Rebound, partial adhesion, splashing, and secondary breakup are not considered.

Brownian diffusion and electrostatic forces are also not explicitly included. These omitted mechanisms are expected to have a greater influence on the predicted capture of the smallest particles. Previous studies have shown that the droplet-to-particle size ratio and impact velocity can affect particle spreading and encapsulation [26]. A post-collision adhesion criterion based on impact and wetting conditions should be added in future model development. Factors such as the impact velocity, droplet-to-particle size ratio, contact angle, surface tension, and dust wettability could also be considered. Such criteria would distinguish geometric collision from stable wet capture [42].

The present validation uses granite dust and compares only the overall pressure-dependent capture trend; it should not be interpreted as direct validation of coal-specific surface interactions. In addition, each numerical case uses a single stochastic realization with 2000 sampled dust particles and 2000 sampled spray particles. Repeated simulations with different random seeds and sampled-particle-number sensitivity tests are therefore required to quantify stochastic uncertainty. Future experimental validation should also include coal dust and the respirable particle-size range.

5. Conclusions

This study developed a weighted DSMC particle framework for spray dust suppression in the external spraying region of a roadheader. The framework was used to analyze the effects of the water pressure, droplet-size distribution, dust-particle size, atomization angle, and spray incidence angle on dust capture. The main conclusions are as follows:

(1) The weighted DSMC model explicitly samples droplet–dust collisions and represents capture and agglomeration using statistical particle weights. The model reproduces the measured pressure-dependent macroscopic capture trend, with relative deviations below 3% at 6–10 MPa.

(2) Increasing water pressure increases spray velocity and droplet number density and shifts the main collision region toward the dust source. Capture efficiency increases from 43.8% at 2 MPa to 80.0% at 6 MPa and 91.6% at 10 MPa, while the incremental gain decreases above 6 MPa and water consumption continues to increase.

(3) A narrower Rosin–Rammler droplet-size distribution increases the represented droplet number density and capture efficiency. Under the present model assumptions, the 0–10 μm class has the lowest collision-controlled capture fraction, while the larger size classes show weaker size dependence in the reported runs.

(4) The atomization angle governs a trade-off between local collision density and spray coverage. Smaller angles concentrate droplets along the spray path and increase local collision density, whereas larger angles expand the collision region but reduce local droplet density and the initial capture rate.

(5) Lower spray incidence angles favor near-source capture, whereas larger incidence angles increase interception across the dust-transport path. Within the tested geometry and operating conditions, the highest final capture efficiency was obtained at 50°, with a slight decrease at 60°.

Author Contributions: Conceptualization, J.Y. and D.M.; methodology, Q.L. and J.Y.; software, Q.L. and Y.K.; validation, Q.L., Y.K. and X.Z.; formal analysis, Q.L.; investigation, Q.L. and Y.K.; resources, J.Y., X.Z., J.F. and D.M.; data curation, Q.L.; writing—original draft preparation, Q.L.; writing—review and editing, J.Y., Y.K., X.Z., J.F. and D.M.; visualization, Q.L. and Y.K.; supervision, J.Y. and D.M.; project administration, J.Y. and D.M.; funding acquisition, J.Y. and D.M. All authors have read and agreed to the published version of the manuscript.

Funding: This research was funded by the National Natural Science Foundation of China, grant number 52304104, and the Fundamental Research Funds for the Central Universities, grant number 2025ZDPYQA1001.

Data Availability Statement: The original contributions presented in this study are included in the article. Further inquiries can be directed to the corresponding authors.

Conflicts of Interest: Author Xue'an Zhuang was employed by the company China Coal Technology and Engineering Group Chongqing Research Institute Co., Ltd. The remaining authors declare that the research was conducted in the absence of any commercial or financial relationships that could be construed as potential conflicts of interest.

References

1. Liu, T.; Liu, S. The impacts of coal dust on miners' health: A review. *Environ. Res.* **2020**, *190*, 109849. [CrossRef] [PubMed]
2. Shekarian, Y.; Rahimi, E.; Rezaee, M.; Roghanchi, P. A systematic review of occupational exposure to respirable coal mine dust (RCMD) in the U.S. mining industry. *Int. J. Coal Sci. Technol.* **2023**, *10*, 29. [CrossRef]
3. Blackley, D.J.; Reynolds, L.E.; Short, C.; Carson, R.; Storey, E.; Halldin, C.N.; Laney, A.S. Progressive massive fibrosis in coal miners from 3 clinics in Virginia. *JAMA* **2018**, *319*, 500–501. [CrossRef] [PubMed]
4. Fan, J.-N.; Deng, J.; Xiao, Y. Comprehensive review of spray and ventilation technologies for coal dust control at mining faces. *Process Saf. Environ. Prot.* **2025**, *195*, 106799. [CrossRef]
5. Zhou, Q.; Qin, B. Coal dust suppression based on water mediums: A review of technologies and influencing factors. *Fuel* **2021**, *302*, 121196. [CrossRef]
6. Li, S.; Zhao, B.; Lin, H.; Shuang, H.; Kong, X.; Yang, E. Review and prospects of surfactant-enhanced spray dust suppression: Mechanisms and effectiveness. *Process Saf. Environ. Prot.* **2021**, *154*, 410–424. [CrossRef]
7. Zhou, Q.; Qin, B.; Ma, D.; Jiang, N. Novel technology for synergetic dust suppression using surfactant-magnetized water in underground coal mines. *Process Saf. Environ. Prot.* **2017**, *109*, 631–638. [CrossRef]
8. Jiang, J.; Wang, P.; Pei, Y.; Liu, R.; Liu, L.; He, Y. Preparation and performance analysis of a coking coal dust suppressant spray. *Int. J. Coal Sci. Technol.* **2021**, *8*, 1003–1014. [CrossRef]
9. Zhao, Z.; Chang, P.; Xu, G.; Ghosh, A.; Morla, R. Experimental study of surfactants' performance for suppressing coal dust with respirable size. *Fuel* **2023**, *352*, 129035. [CrossRef]
10. Zhao, Z.; Chang, P.; Ghosh, A.; Xu, G.; Liu, Y.; Morla, R. The influence of surfactants' ionicity on the performance of coal dust suppression. *Adv. Powder Technol.* **2024**, *35*, 104295. [CrossRef]
11. Niu, W.; Nie, W.; Bao, Q.; Tian, Q.; Li, R.; Zhang, X.; Yan, X.; Lian, J. Development and characterization of a high efficiency bio-based rhamnolipid compound dust suppressant for coal dust pollution control. *Environ. Pollut.* **2023**, *330*, 121792. [CrossRef] [PubMed]
12. Liu, Z.; Nie, W.; Peng, H.; Yang, S.; Chen, D.; Liu, Q. The effects of the spraying pressure and nozzle orifice diameter on the atomizing rules and dust suppression performances of an external spraying system in a fully-mechanized excavation face. *Powder Technol.* **2019**, *350*, 62–80. [CrossRef]
13. Ma, D.; Yan, J.; Liu, Q.; Li, Q.; Zhang, C. Hard rock cuttability enhancement using fracture interfaces: Role of confining pressure. *Rock Mech. Rock Eng.* 2026; *online first*. [CrossRef]
14. Xu, C.; Nie, W.; Liu, Z.; Peng, H.; Yang, S.; Liu, Q. Multi-factor numerical simulation study on spray dust suppression device in coal mining process. *Energy* **2019**, *182*, 544–558. [CrossRef]
15. Ma, Q.; Nie, W.; Yang, S.; Xu, C.; Peng, H.; Liu, Z.; Guo, C.; Cai, X. Effect of spraying on coal dust diffusion in a coal mine based on a numerical simulation. *Environ. Pollut.* **2020**, *264*, 114717. [CrossRef] [PubMed]
16. Guo, C.; Nie, W.; Xu, C.; Peng, H.; Zhang, C.; Li, S.; Yue, N.; Liu, Z.; Yang, S.; Ma, Q.; et al. A study of the spray atomization and suppression of tunnel dust pollution based on a CFD-based simulation. *J. Clean. Prod.* **2020**, *276*, 123632. [CrossRef]
17. Peng, H.; Nie, W.; Liu, Z.; Xiu, Z.; Yang, S.; Xu, C.; Ma, Q.; Guo, C. Optimization of external spray negative-pressure mist-curtain dust suppression devices for roadheaders based on a multi-factor orthogonal experiment. *J. Clean. Prod.* **2020**, *275*, 123603. [CrossRef]
18. Peng, H.; Nie, W.; Yu, H.; Cheng, W.; Bai, P.; Liu, Q.; Liu, Z.; Yang, S.; Xu, C.; Hua, Y.; et al. Research on mine dust suppression by spraying: Development of an air-assisted PM10 control device based on CFD technology. *Adv. Powder Technol.* **2019**, *30*, 2588–2599. [CrossRef]
19. Hu, S.; Huang, Y.; Feng, G.; Shao, H.; Liao, Q.; Gao, Y.; Hu, F. Investigation on the design of atomization device for coal dust suppression in underground roadways. *Process Saf. Environ. Prot.* **2019**, *129*, 230–237. [CrossRef]
20. Zhou, Q.; Qin, B.; Wang, F.; Wang, H.; Hou, J.; Wang, Z. Effects of droplet formation patterns on the atomization characteristics of a dust removal spray in a coal cutter. *Powder Technol.* **2019**, *344*, 570–580. [CrossRef]
21. Zhang, G.; Zhou, G.; Zhang, L.; Sun, B.; Wang, N.; Yang, H.; Liu, W. Numerical simulation and engineering application of multistage atomization dustfall at a fully mechanized excavation face. *Tunn. Undergr. Space Technol.* **2020**, *104*, 103540. [CrossRef]

22. Xie, Y.; Cheng, W.; Yu, H.; Wang, Y. Study on spray dust removal law for cleaner production at fully mechanized mining face with large mining height. *Powder Technol.* **2021**, *389*, 48–62. [CrossRef]
23. Ma, D.; Gao, X.; Zhang, J. Co-exploitation of mine-derived geothermal energy: Recent advances and emerging perspectives. *GeoEnergy Commun.* **2025**, *1*, 12. [CrossRef]
24. Liu, N.; Wu, X.; Deng, E.; Liu, X.; Wang, Y. A U-shaped spray device on a front boom-type roadheader for dust suppression in a metro tunnel. *Sustain. Cities Soc.* **2023**, *89*, 104369. [CrossRef]
25. Peng, H.; Nie, W.; Zhang, X.; Xu, C.; Meng, X.; Cheng, W.; Liu, Q.; Hua, Y. Research on the blowing-spraying synergistic dust removal technology for clean environment in large-scale mechanization coal mine. *Fuel* **2022**, *324*, 124508. [CrossRef]
26. Xu, C.; Nie, W.; Peng, H.; Zhang, S.; Liu, F.; Yi, S.; Cha, X.; Mwabaima, F.I. Numerical simulation of the dynamic wetting of coal dust by spray droplets. *Energy* **2023**, *270*, 126667. [CrossRef]
27. Nie, W.; Li, J.; Peng, H.; Xu, C.; Zhang, S.; Cha, X.; Yi, S.; Mwabaima, F.I. Study of spray atomization law and dust suppression effect of a wet dust catcher on a hydraulic support. *Energy* **2024**, *305*, 132296. [CrossRef]
28. Ren, S.; Jing, D.; Ge, S.; Chen, Y.; Chang, P. Investigate the optimum design of atomizing nozzles for coal dust suppression by using multifactor level response surface methodology. *Process Saf. Environ. Prot.* **2024**, *190*, 245–261. [CrossRef]
29. Chen, X.; Bai, X.; Fan, C.; Ge, S.; Deng, C.; Ma, G. Experimental investigation of atomization characteristics of sonic blasting nozzle based on De-Laval dynamics. *Energy* **2024**, *297*, 131188. [CrossRef]
30. Han, H.; Wang, H.; Zhang, Q.; Du, Y.; Wang, H.; Wang, H. Investigations of the effects of two typical jet crushing methods on the atomization and dust reduction performance of nozzles. *Int. J. Coal Sci. Technol.* **2023**, *10*, 50. [CrossRef]
31. Pawar, S.K.; Padding, J.T.; Deen, N.G.; Jongsma, A.; Innings, F.; Kuipers, J.A.M. Numerical and experimental investigation of induced flow and droplet–droplet interactions in a liquid spray. *Chem. Eng. Sci.* **2015**, *138*, 17–30. [CrossRef]
32. Finotello, G.; Padding, J.T.; Buist, K.A.; Jongsma, A.; Innings, F.; Kuipers, J.A.M. Droplet collisions of water and milk in a spray with Langevin turbulence dispersion. *Int. J. Multiph. Flow* **2019**, *114*, 154–167. [CrossRef]
33. Zhao, H.; Fan, F.; Su, J.; Hu, X.; Su, M. An improved DSMC method for acoustic agglomeration of solid particles assisted by spray droplets. *Int. J. Multiph. Flow* **2024**, *176*, 104829. [CrossRef]
34. Fede, P.; Simonin, O.; Villedieu, P. Monte-Carlo simulation of colliding particles or coalescing droplets transported by a turbulent flow in the framework of a joint fluid–particle PDF approach. *Int. J. Multiph. Flow* **2015**, *74*, 165–183. [CrossRef]
35. Bird, G.A. *Molecular Gas Dynamics and the Direct Simulation of Gas Flows*; Oxford University Press: Oxford, UK, 1994. [CrossRef]
36. Schiller, L.; Naumann, A. A drag coefficient correlation. *Z. Ver. Dtsch. Ing.* **1933**, *77*, 318–320. [CrossRef] [PubMed]
37. Glasserman, P.; Yao, D.D. Some guidelines and guarantees for common random numbers. *Manag. Sci.* **1992**, *38*, 884–908. [CrossRef]
38. Galitzine, C.; Boyd, I.D. An analysis of the convergence of the direct simulation Monte Carlo method. *J. Comput. Phys.* **2015**, *289*, 196–223. [CrossRef]
39. Lefebvre, A.H.; McDonell, V.G. *Atomization and Sprays*, 2nd ed.; CRC Press: Boca Raton, FL, USA, 2017. [CrossRef]
40. Vesilind, P.A. The Rosin–Rammler particle size distribution. *Resour. Recovery Conserv.* **1980**, *5*, 275–277. [CrossRef]
41. Beck, T.W.; Seaman, C.E.; Shahan, M.R.; Mischler, S.E. Open-air sprays for capturing and controlling airborne float coal dust on longwall faces. *Min. Eng.* **2018**, *70*, 42–48. [CrossRef] [PubMed]
42. Shams Taleghani, A.; Sheikholeslam Noori, M. Numerical investigation of coalescence phenomena, affected by surface acoustic waves. *Eur. Phys. J. Plus* **2022**, *137*, 975. [CrossRef]

Disclaimer/Publisher's Note: The statements, opinions and data contained in all publications are solely those of the individual author(s) and contributor(s) and not of MDPI and/or the editor(s). MDPI and/or the editor(s) disclaim responsibility for any injury to people or property resulting from any ideas, methods, instructions or products referred to in the content.